A STRETCHABLE NEURAL INTERFACE FOR VAGUS NERVE STIMULATION: FABRICATION AND ELECTROCHEMICAL CHARACTERIZATION

Jongcheon Lim[1,2,3], Matthew P Ward[1,2,3,4], John B Furness[5], Luis C Populin[6], and Hyowon Lee[1,2,3]*
[1]Weldon School of Biomedical Engineering, Purdue University, West Lafayette, IN, USA
[2]Birck Nanotechnology Center, Purdue University, West Lafayette, IN, USA
[3]Center for Implantable Devices, Purdue University, West Lafayette, IN, USA
[4]Indiana University School of Medicine, Indianapolis, IN, USA
[5]Department of Physiology and Anatomy, University of Melbourne, Parkville, Vic, Australia
[6]Department of Neuroscience, University of Wisconsin-Madison, Madison, WI, USA

ABSTRACT
Soft, stretchable design can improve long-term stability of neural interface devices. Here we present our latest efforts to design, fabricate and evaluate stretchable thin-film cuff electrode devices for vagus nerve stimulation, which have Y-shaped kirigami microstructures. We fabricated stretchable Y- microstructured thin-film cuff electrodes by using conventional photolithography and reactive ion etching. The monolithic device design enables easier transfer to a different substrate without having to use the traditional PDMS-stamp-based transfer printing technique. We then characterized the electrochemical properties of the electrode/electrolyte interface and evaluated the charge injection limits as stimulating neural electrodes. Although the microstructured electrodes show up to 3.68 times higher impedance than the Euclidean geometry electrode due to the reduced surface area, they show up to 2.13 times higher charge storage capacities and 12.1 % higher charge injection limits, which may be useful for a chronic neural interface.

KEYWORDS
Vagus Nerve Stimulation, Stretchable, Kirigami, Neural Interface.

INTRODUCTION
Vagus nerve stimulation (VNS) is an effective method to treat neurological disorders such as drug-resistant epilepsy and depression. It is also known to be therapeutic for other inflammatory diseases such as inflammatory bowel disease (IBD) [1]. Slowly conducting (<1 m/s) unmyelinated C-fibers in the vagus nerve are thought to drive the anti-inflammatory effects of those diseases [2]. Previously, a study reported applying VNS in a sheep model to treat IBD by using a silicone-based flat interface nerve electrode (FINE) [2]. FINE ensures good contact between the electrode and nerve by applying moderate pressure to maximize stimulation efficiency for C-fibers, which are known to have a higher activation threshold than other types of myelinated fibers [3], by maintaining intimate electrode-to-nerve distance. However, this interface can potentially damage the nerve if it applies pressure higher than 30 mm Hg to flatten the fascicle [4]. Moreover, the silicone wall of the FINE cuff is thick (thickness = 0.5-0.8 mm), which can apply restrictive mechanical forces to the nerve or surrounding tissue due to its volume. The volumetric footprint around the nerve can be reduced by making the cuff with a flexible thin-film substrate such as polyimide (PI). Even though PI thin-film substrates are flexible, they have a GPa range of Young's modulus and the cylindrical geometry from the cuffing can add even more structural rigidity, which can potentially damage the nerve by the mismatching mechanical behavior under ambient motion. The issue can be mitigated by making the PI substrate stretchable. Vachicouras *et al.* (2019) suggested a strategy to make the PI stretchable by making a Y-shaped kirigami pattern to the substrate [5]. However, they used relatively expensive methods, such as ion-milling, to fabricate complex geometry.

Herein we present a relatively conventional microfabrication process to make the Y-shaped kirigami patterned structure for a more compliant and reliable interface for vagus nerve stimulation. Furthermore, we investigated whether there are any improvements in electrochemical characteristics of the electrode/electrolyte interface for the Y-shaped kirigami patterned electrodes, which have a higher perimeter to surface area (PSA) ratio than the rectangular electrode geometry. A previous study on microelectrodes with high PSA electrode geometry, such as Vicsek fractal geometry, suggests that the charge injection limit can be enhanced by improving the diffusion-limited Faradaic charge interactions [6]. We conducted experiments to determine whether similar performance improvement may apply to macroelectrodes with microstructures.

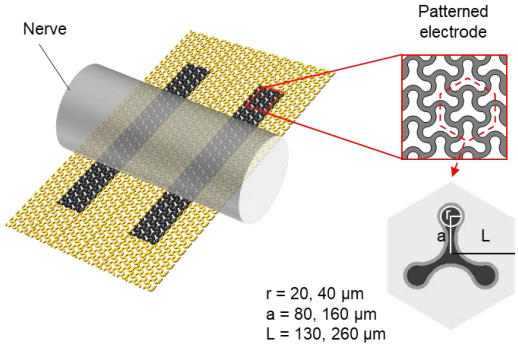

Figure 1: Schematic illustration of the concept of a stretchable thin-film cuff electrode device based on a Y-shaped kirigami structure

MATERIALS AND METHODS
Design of the Device
We chose the Y-shaped kirigami pattern based on literature in which the mechanical properties resulting from design parameters (r, a, L) were experimentally optimized to increase overall compliance against tensile strain (Figure 1) [5]. In this work, we made two versions of the peripheral nerve interface which we named "r20" and "r40". The first, r20, used shape parameters: r = 20 µm; a = 80 µm; L = 130 µm. The second version, r40, has design parameters increased by a factor of two. Figure 2 shows the layout of the device with important dimensions annotated. The entire device except for the contact pad part is perforated with a Y-shaped kirigami hole pattern. The electrode contact dimensions were determined based on the diameter of the rhesus macaque's cervical vagus nerve, which is known to be around 2 mm [7]. We adopted the multi bipolar cuff array design from a previous study that used FINE [2]. The device has three cuffs: one stimulation electrode, which is the first cuff from the left in Figure 2, and two recording electrodes with different conduction distances (10 mm and 20 mm).

978-1-940470-04-7/HH2022/$25©2022TRF
DOI 10.31438/trf.hh2022.26

The purpose of having an array of recording electrodes is to better identify electrically evoked compound action potential volleys with different conduction velocities. The extra space in the flaps of the cuff can be used for handling the device and for the closure mechanism by suturing them together or applying self-adhesive glue or gel. The contact pads are designed to be compatible with ZIF-clip headstage connectors (Tucker-Davis Technologies, Alachua, FL, USA).

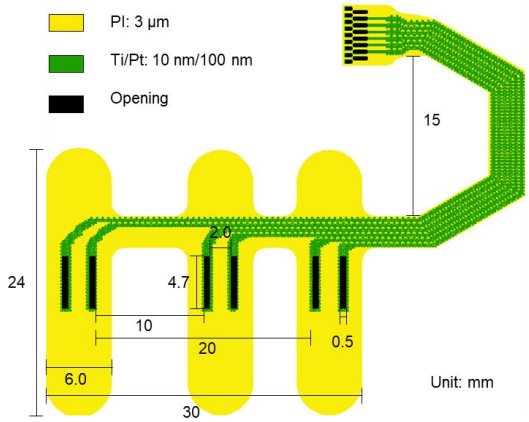

Figure 2: Layout of the device with important dimensions annotated.

Device Fabrication

Figure 3 shows the fabrication process. The PI resin (PI 2545, HD Microsystems, Parlin, NJ) was spin-coated (thickness = 1.5 µm) and cured on a 100-mm silicon wafer at 300 °C. A positive photoresist (PR, AZ9260, MicroChem, Newton, MA, USA) was used to make the metal trace pattern. We used a maskless aligner (MLA150, Heidelberg Instruments, Germany) for the exposure and alignment processes. After the 1st photolithography, the wafer was sputtered with 10 nm of titanium (Ti) and 100 nm of platinum (Pt) followed by a lift-off process. Another PI layer (thickness = 1.5 µm) was cured on the wafer as a passivation layer. The wafer was coated with a thicker layer (~20 µm) of PR by spinning and baking twice for the 2nd photolithography. The pattern was aligned by using an automatic alignment feature of MLA150. After the exposure and development, we used the reactive ion etch (RIE) process with oxygen plasma (50 sccm at 100 W in 50 mTorr for 60 min) to define the outline of the device. The same process was repeated in the 3rd photolithography and RIE for the opening of the electrodes. After visual observation under the microscope, the device was released from the wafer by partially etching the silicon with a buffered oxide etch within 15 min and rinsed 5 times with de-ionized water, then transferred to another substrate using water for further handling.

Electrochemical Characterizations

We conducted cyclic voltammetry (CV) and electrochemical impedance spectroscopy (EIS) in phosphate-buffered saline (PBS, ThermoFisher Scientific, MA, USA) solution using a potentiostat (SP-200, Bio-Logic Inc, Seyssinet-Pariset, France) with three-electrode configuration: Electrode contact of the device as a working electrode, graphite counter electrode and Ag/AgCl with 3 M KCl reference electrode (RE-1CP, ALS Co. Ltd., Tokyo, Japan). CV was scanned between -0.6 V and 0.8 V versus the reference electrode with a scan rate of 50 mV/s. GSAs of the No microstructure, r40 and r20 are 2.35 mm^{-1}, 0.899 mm^{-1}, and 0.969 mm^{-1} respectively, and were used to calculate the current density.

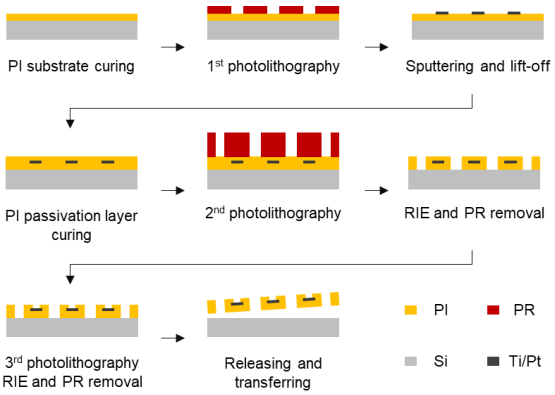

Figure 3: Schematic illustrations of the fabrication process of the device

Voltage Transient Measurements

We conducted voltage transient measurements using a stimulus isolator (BSI-1A, BAK Electronics, Inc, Umatlla, FL. USA) in the same experiment setup used for the electrochemical characterizations. We used a cathodic-first alternating monophasic current-controlled stimulus waveform. The pulse repetition frequency, train duration, and pulse duration were set at 50 Hz, 1 sec, and 1 ms, respectively. The current pulse was monitored by measuring voltage between 100-Ω-resistor, which is connected in series to the stimulator. Data was acquired via an I/O device (USB-6361, National Instruments, Austin, TX, USA).

RESULTS AND DISCUSSION

Figure 4a shows the device as fabricated on the wafer substrate. The entire body of the device is monolithically constructed and can be transferred to another substrate without having to use the PDMS-stamp-based transfer printing technique, which is traditionally used to transfer stretchable thin-film interconnect patterns but requires proficiency for successful results. Our device maintains its shape when it's floating on the surface of the water.

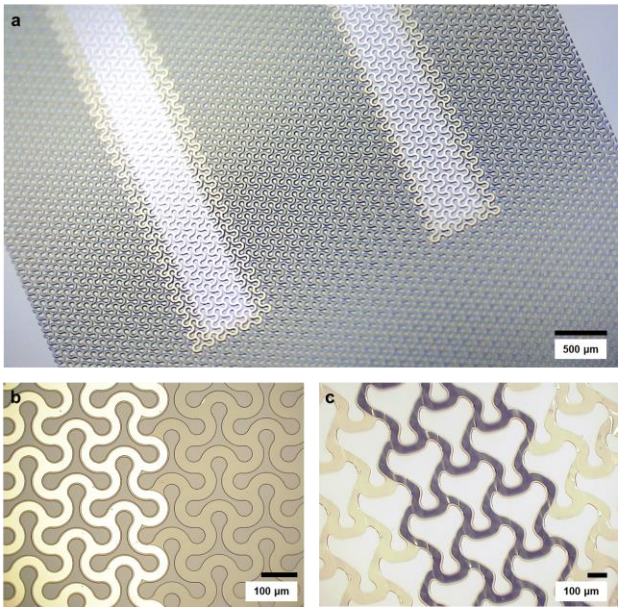

Figure 4: Representative images of the fabricated device. (a) The fabricated device on a silicon wafer. Optical microscope images of the device after transferring to a glass substrate (b) and mechanically stretched (c).

After gently being placed on a wet glass substrate, the substrate can be inclined at a certain angle to make the drying front formed at the top and to recede directionally below, so that the device can be transferred flat on the glass substrate. Figure 4b shows an optical microscopy image of the device after it is transferred to a glass substrate. We did not observe any notable damage on the device after the transfer. The device is stretchable due to the Y-shaped kirigami structure as it is shown in Figure 4c.

Results of CV and EIS Measurements

Figure 5a shows representative CV plots of the electrodes. All three electrodes show representative characteristic electrochemical reactions at the Pt/PBS interface: Current densities increase toward 0.8 V from the oxidation of Pt, and negative peaks appear between -0.2-0 V from the reduction of Pt. From the CV measurements, we can compare cathodic charge storage capacity (CSC_c), which is a measure of total injectable charge density at a near-equilibrium condition. We calculated CSC_c from the charge storage capacity (CSC) of voltammograms using the following equation [8]:

$$CSC = \frac{1}{\nu A}\int_{E_c}^{E_a} |i| dE \; (C/cm^2) \quad (1)$$

Where E is potential versus Ag/AgCl reference electrode; i is measured current; E_a and E_c are positive and negative potential limits; A is GSA, and ν is the scan rate. Figure 5c shows the mean and standard deviation of CSC_c for the electrodes (N=6, each electrode). r20 shows the highest CSC_c (3.65 ± 0.377 mC cm^{-2}) compared to r40 (2.39 ± 0.188 mC cm^{-2}) and the electrode without microstructure (1.71 ± 0.128 mC cm^{-2}). That is, r20 can inject the most charge density at a near-equilibrium condition where the charge is injected sufficiently slow to let faradaic charge interaction and double-layer charging occur throughout the entire electrode region. The higher overall current density from the CV of r40 and r20 could be attributed to the increased perimeter of the microstructured electrodes, where we expect a higher current density than the central region. A more detailed investigation of the spatial current density profile should be made in the future to further analyze the effect of the increased perimeter of the electrodes. Figure 5b shows representative Bode plots from the EIS. Impedance values (mean and standard deviation, N=6, each electrode) at 1 kHz were plotted in Figure 5d for a comparison. r40 and r20 have higher impedance at 1 kHz, which are 2.58 ± 0.562 kΩ and 2.42 ± 0.332 kΩ respectively compared to that of the electrode without microstructure, which is 0.701 ± 0.120 kΩ. It is important to note that r40 and r20 have 0.383- and 0.412-times smaller GSAs respectively compared to the electrode without microstructure.

Results of Voltage Transient Measurements

We conducted voltage transient measurements to estimate charge injection limits for the electrodes. Figure 6a shows representative voltage transients (solid lines) of a cathodic phase and the following charge balancing anodic phase along with the monitored current pulse (blue dashed line) at 1 mA of pulse current amplitude and 1 ms of pulse duration. Maximum cathodic potential excursion (E_{mc}) was estimated by taking the potential value at the point where the actual current pulse ends as shown in the inset of Figure 6a. We investigated E_{mc} for all the electrodes at pulse current amplitudes between 0 mA to 2 mA (Figure 6b). Mean and standard deviation was obtained from 50 stimuli at each pulse current amplitude. Charge injection limits were interpolated from the intercepts of lines drawn by mean E_{mc} and the cathodic electrolysis limit of water at the surface of Pt (brown dashed horizontal line) [8].

The estimates are organized in Table 1. Although the maximum current amplitudes at the cathodic limit for r40 (0.494 mA) and r20 (0.459 mA) were almost two-fold smaller than that of the electrode without microstructure (1.06 mA), estimated charge injection limits were higher for r40 (0.0550 mC cm^{-2}) and r20 (0.0474 mC cm^{-2}) compared to the electrode without microstructures (0.0453 mC cm^{-2}) due to the smaller GSAs. It is important to note that the GSA of the electrodes is around 1 mm^2 range; therefore, regarded as macroelectrodes rather than microelectrodes, which have a GSA of around 5,000 μm^2 [8]. Macroelectrodes have an order of magnitude lower charge injection limit than microelectrodes because they have a larger underutilized central region, where transport of ions is more limited than the perimeter [8].

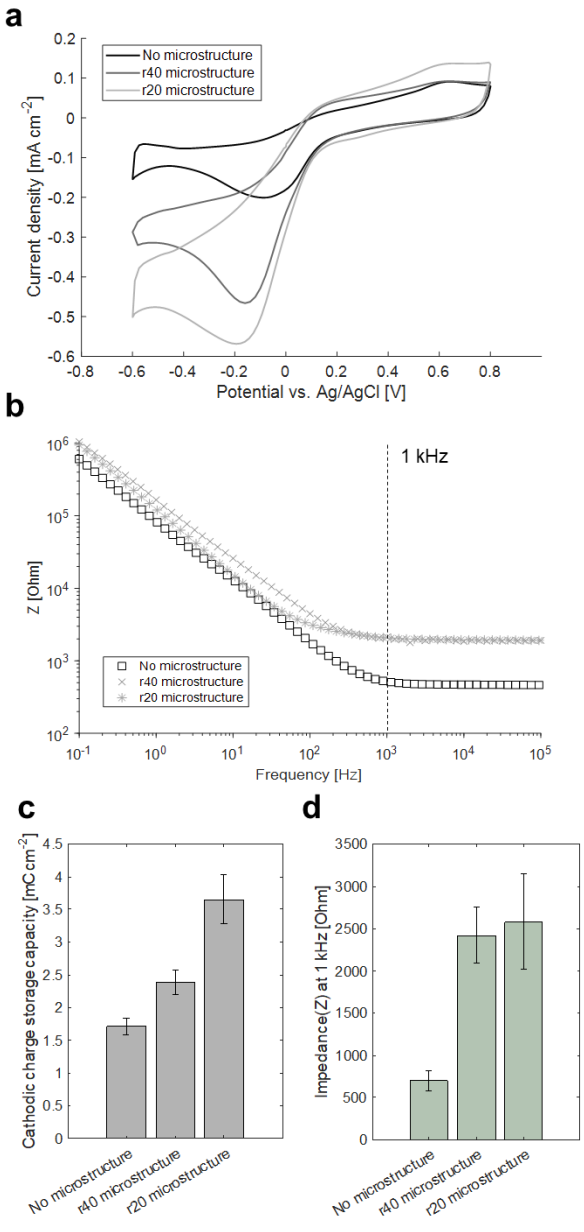

Figure 5: Electrochemical characterization of the electrodes in PBS solution: (a) CV plots. (b) EIS Bode plots. (c-d) CSC_c (c), and impedance at 1 kHz (d) for different designs of electrodes (N=6, each).

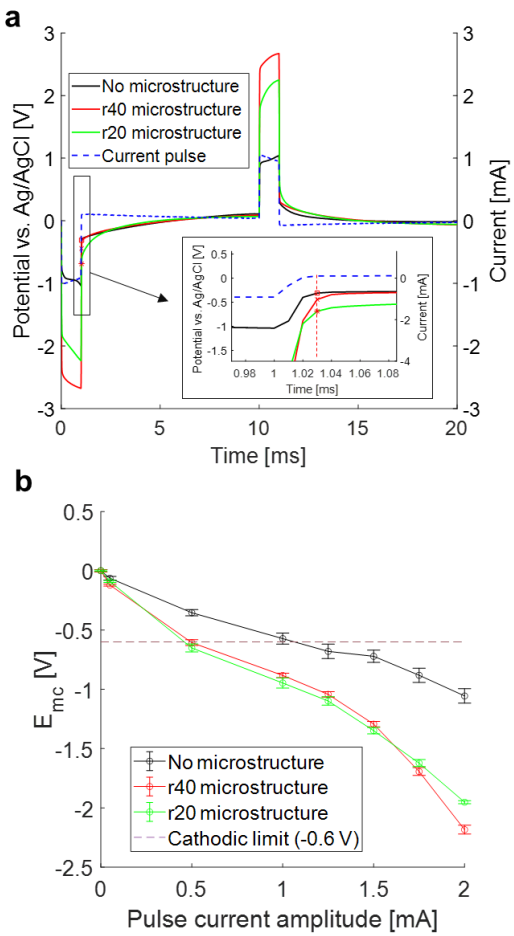

Figure 6: Voltage transient analysis: (a) Representative voltage transient plot for each type of electrode. (b) Estimated E_{mc}s for the different designs of electrodes.

Table 1: GSA and charge injection limit of each electrode design.

	No μstructure	r40 μstructure	r20 μstructure
GSA (mm^{-2})	2.35	0.899	0.969
Charge injection limit ($mC\ cm^{-2}$)	0.0453	0.0550	0.0474

Summary and Future Plan

We found that the kirigami structure reduces the GSA of the electrode thereby increasing the impedance, yet results in the enhancement of CSC_c, which is a measure of the total charge available for a stimulating electrode [8]. The results from voltage transient measurements suggest that the kirigami structured electrodes perform slightly better than non-structured Pt electrodes in terms of charge injection limit. This result agrees with a previous study in our group, which suggests that electrodes with high PSA geometry, such as Vicseck fractal geometry, show enhancement of charge injection limit [6]. However, it is not clear whether the diffusion-limited Faradaic charge transfer is significantly improved in this stretchable electrode design, which features macroelectrodes with microstructures. We expect the performance may be further enhanced by coating the surface of the electrode with platinum-iridium (Pt-Ir) alloy or iridium oxide (IrO_2). We also expect these microscale patterns will accelerate the corrosion of the Pt electrodes. This may be mitigated potentially by using Pt-Ir or IrO_2 coating or a layer of graphene [9]. We plan to conduct tensile testing while measuring the electrical conductivity to characterize the electromechanical responsiveness of the stretchable conductive traces of the device along with the electrical and/or mechanical failure limits. Local stress applied by the global stretch of the kirigami pattern can be analyzed by conducting finite element analyses. Furthermore, we plan to quantify any functional benefit of these stretchable peripheral interfaces *in vivo* and identify potential failure modes of the device. Ultimately, we expect to use the device we developed for advanced studies of VNS for the treatment of IBD as well as for neuromodulations of various other parts of the autonomic nervous system.

ACKNOWLEDGEMENTS

This work was supported by the NIH SPARC OT2 OD023847 project.

REFERENCES

[1] J. Meregnani, D. Clarençon, M. Vivier, A. Peinnequin, C. Mouret, V. Sinniger, C. Picq, A. Job, F. Canini, M. Jacquier-Sarlin, and B. Bonaz, "Anti-inflammatory effect of vagus nerve stimulation in a rat model of inflammatory bowel disease." *Autonomic Neuroscience* 160.1-2 (2011): 82-89.

[2] S.C. Payne, O. Burns, M. Stebbing, R. Thomas, A.D. Silva, A. Sedo, F. Weissenborn, T. Hyakumura, M. Huynh, C.N. May, and R.A. Williams, "Vagus nerve stimulation to treat inflammatory bowel disease: a chronic, preclinical safety study in sheep." *Bioelectronics in Medicine* 1.4 (2018): 235-250.

[3] R.M. McAllen, A.D. Shafton, B.O. Bratton, D. Trevaks, and J.B. Furness, "Calibration of thresholds for functional engagement of vagal A, B and C fiber groups in vivo." *Bioelectronics in medicine* 1, no. 1 (2018): 21-27.

[4] D.J. Tyler, and D.M. Durand, "Chronic response of the rat sciatic nerve to the flat interface nerve electrode. *Annals of biomedical engineering*, *31*(6), pp.633-642 (2003).

[5] N. Vachicouras, O. Tarabichi, V.V. Kanumuri, C.M. Tringides, J. Macron, F. Fallegger, Y. Thenaisie, L. Epprecht, S. McInturff, A.A. Qureshi, and V. Paggi, "Microstructured thin-film electrode technology enables proof of concept of scalable, soft auditory brainstem implants." *Science translational medicine* 11.514 (2019).

[6] H. Park, P. Takmakov, and H. Lee. "Electrochemical evaluations of fractal microelectrodes for energy efficient neurostimulation." *Scientific reports* 8, no. 1 (2018): 1-11.

[7] M.L. Settell, N.A. Pelot, B.E. Knudsen, A.M. Dingle, A.L. McConico, E.N. Nicolai, J.K. Trevathan, J.A. Ezzell, E.K. Ross, K.J. Gustafson, and A.J. Shoffstall, "Functional vagotopy in the cervical vagus nerve of the domestic pig: implications for the study of vagus nerve stimulation." *Journal of neural engineering* 17, no. 2 (2020): 026022.

[8] S.F. Cogan, "Neural stimulation and recording electrodes." *Annu. Rev. Biomed. Eng.* 10 (2008): 275-309.

[9] H. Park, S. Zhang, A. Steinman, Z. Chen, and H. Lee. "Graphene prevents neurostimulation-induced platinum dissolution in fractal microelectrodes." *2D Materials* 6, no. 3 (2019): 035037.

CONTACT

*H. Lee, hwlee@purdue.edu